Off-axis electron holography of unstained bacteriophages: Towards electrostatic potential measurement of biological samples

Elio Karim, Christophe Gatel, Amélie Leforestier, Stéphanie Balor, Vanessa Soldan, Célia Plisson-Chastang, Pierre-Emmanuel Gleizes, Etienne Snoeck

Off-axis electron holography of unstained bacteriophages: toward electrostatic potential measurement of biological samples

Elio KARIM[a,b]d, Christophe GATEL[a], Amélie LEFORESTIER[c], Stéphanie BALOR[b], Vanessa SOLDAN[b], Célia PLISSON-CHASTANG[b], Pierre-Emmanuel GLEIZES[b]*, Etienne SNOECK[a]*

[a]CEMES-CNRS, Université de Toulouse, I3EM Team, 29 rue Jeanne Marvig B.P. 94347 31055 Toulouse, France
[b]MCD and METi, Centre de Biologie Intégrative, Université de Toulouse, CNRS, 169 Avenue Marianne Grunberg-Manago, 31062 Toulouse, France
[c]LPS-Université Paris-Saclay, CNRS UMR 8502, Bât. 510, 91405 Orsay Cedex – France
ORCID ID: 0009-0008-3462-4678;
d Current first author address: Univ. Grenoble Alpes, CEA, CNRS, Institut de Biologie Structurale (IBS), Grenoble, France.
Corresponding authors e-mails: etienne.snoeck@cemes.fr; pierre-emmanuel.gleizes@univ-tlse3.fr

1. Abstract

Transmission electron microscopy, especially at cryogenic temperature, is largely used for studying biological macromolecular complexes. A main difficulty of TEM imaging of biological samples is the weak amplitude contrasts due to electron diffusion on light elements that compose biological organisms. Achieving high-resolution reconstructions implies therefore the acquisition of a huge number of TEM micrographs followed by a time-consuming image analysis. This TEM constraint could be overcome by extracting the phase shift of the electron beam having interacted with a "low contrast" sample. This can be achieved by off-axis electron holography, an electron interferometric technique used in material science, but rarely in biology due to lack of sensitivity. Here, we took advantage of recent technological advances on a dedicated 300 keV TEM to re-evaluate the performance of off-axis holography on unstained T4 and T5 bacteriophages at room temperature and in cryogenic conditions. Our results demonstrate an improvement in contrast and signal-to-noise ratio at both temperatures compared to bright field TEM images, with some limitations in spatial resolution. In addition, we show that the electron beam phase shift gives information on charge variations, paving the way to electrostatic potential studies of biological objects at the nanometer scale.

Keywords
- Off-axis electron holography
- Phase imaging
- High-contrast imaging
- Electrostatic potential measurements
- Cryo-EM
- Phase objects

2. Introduction

Transmission electron microscopy (TEM) is a major technique used for biological objects imaging. The first electron microscope developed by Ernst Ruska and Max Knoll (Ortiz Ortega et al., 2022) was used for cell imaging and led to the observation of various biological samples starting with bacteriophages

(Peankuch and Kausche, 1940; Ruska, 1940). It was however clear that biological specimens exhibit a very weak inherent TEM contrast due to the low atomic number of the chemical elements that compose biological materials, like C, N, H, O and P, resulting in a weak change of the incident electron wave amplitude after interaction (Simon et al., 2008). This weak amplitude contrast cannot be overcome by increasing the electron dose because of the high sensitivity of biological specimen to electron beam irradiation, which results in damages like sample heating, electrostatic charging, and ionizing damage (radiolysis) (Egerton et al., 2004). To increase the TEM contrast, positive or negative staining approaches were first developed (Brenner and Horne, 1959). These staining methods have the double advantage of enhancing the sample contrast and protecting it against beam damage. They enable the observation of macromolecules with improved resolutions down to 20 to 10 Å at room temperature (RT) (Gallagher et al., 2019). However, interaction of the contrasting agent with the sample may alter its structure, in addition to dehydration required to maintain the TEM vacuum.

Approximately 50 years ago, cryogenic electron microscopy (cryo-EM) was developed to image biological samples in their native environment, without staining or dehydration artifacts (Dubochet and McDowall, 1981). In cryo-EM, the samples in solution are rapidly frozen in vitreous ice and studied at very low temperature (around -175°C). Over the last two decades, cryo-EM has benefited from the breakthrough development of direct detection devices (DDD) (Kühlbrandt, 2014) and software improvements with, for example, the development of Bayesian statistics for 3D particle reconstruction (Scheres, 2012). This has enabled high-resolution structural studies (with spatial resolutions less than 4 Å) and led to the Nobel Prize in Chemistry in 2017 (The Nobel Prize in Chemistry 2017). However, the fine analysis of 3D structures of low-contrast objects still requires recording hundreds to thousands TEM images in order to extract images of 10^5-10^7 macromolecules (particles) (Singer and Sigworth, 2020), which are then classified, selected and averaged to regain sufficient signal-to-noise ratio and reconstruct the 3D volume of the macromolecule at high resolution. This powerful single-particle analysis (SPA) workflow remains then relatively time-consuming and struggles to attain high resolutions with very small or highly flexible proteins (Benjin and Ling, 2020; D'Imprima and Kühlbrandt, 2021).

As already stated, conventional TEM methods like cryo-EM only permit to detect the weak amplitude variations of the electron exit wave while its phase shift is lost (Lichte, 2013). In biological samples, the phase shifts of the electron wave are more significant than the amplitude changes, thus capable of providing higher contrast of the sample if collected. Among various possibilities to retrieve the electron exit wave phase is the electron holography technique. It was proposed in 1947 by Denis Gabor (Gabor, 1948) to retrieve the full information of the amplitude and phase of the exit electron wave condensing at the detector to compensate for all optical aberrations that severely limited the TEM resolution (Tonomura, 1998).

The phase shift experienced by the e-beam, $\varphi(x,y)$, depends on the local electrostatic potential $V(x,y,z)$ and possible magnetic potential through the Aharonov-Bohn equation. Considering only the electrostatic contribution to the phase shift and an electron path along the *z* axis, this equation is:

$$\varphi(x,y) = C_E . \int V(x,y,z)dz \quad (1)$$

C_E being a constant only related to the electron energy.

The local electrostatic potential $V(x,y,z)$ is the addition of the Mean Inner Potential (MIP) of the materials which depends on the local atomic composition, density and ionicity (Cassidy et al., 2017) plus a possible additional electrostatic potential due to local electric charges. To illustrate the contributions of the MIP and of electric charges on the phase shift: a single oxygen atom induces a phase shift of about $2\pi/50$

rad, while an elementary charge produces a phase shift of 2π/100 rad (Lichte, 2013).

The off-axis electron holography set-up, which is presented in this work, consists of interfering the part of the beam going through the object (i.e. the object beam) with one passing through a reference area - vacuum or a constant thickness of low phase shift - (i.e. the reference beam), thanks to the use of an electrostatic biprism (invented by G. Mollenstedt and H. Duker in 1955 (Möllenstedt and Düker, 1955)). The single biprism setup is shown in Figure 1a left. The light blue part is the reference beam and the dark blue is the object beam. A positive potential is applied to the biprism to bend the two beam parts and make them interfere. In this single biprism set-up the higher the biprism voltage, the larger the overlapping area and the smaller the interference fringe spacing. In our work, we used a more sophisticated double biprism setup (Figure 1a right) which allows for independent tuning of the interference fringe spacing which controls the spatial resolution, and of the interference overlapping area which tune the field of view (FOV) wideness (Harada et al., 2004). The interference between the phase shifted exit wave and the reference wave is schematized in Figure 1b. It produces interference fringes (i.e. the hologram) of alternating dark and white fringes (Figure 1b, bottom) whose Fourier analysis allows retrieving the phase shift of the object wave (supplementary text S1). This phase shift information allows the study of different material properties, for example, measuring electrical fields (Gatel et al., 2013), studying magnetic fields (Andersen et al., 2020) or for strain field mapping (Hytch et al., 2011).

In ideal conditions of samples insensitive to beam damage and with a perfect detector, off-axis holography currently can detect phase shifts beyond 2π/1000 (Voelkl and Tang, 2010). To overcome sample and fringe drift and optimize the fringe contrast, fringe stabilization as well as sample drift correction processes and a π-shifting method (Gatel et al., 2018; Hÿtch and Gatel, 2021), have been developed to enable long acquisitions and achieve high SNR phase images.

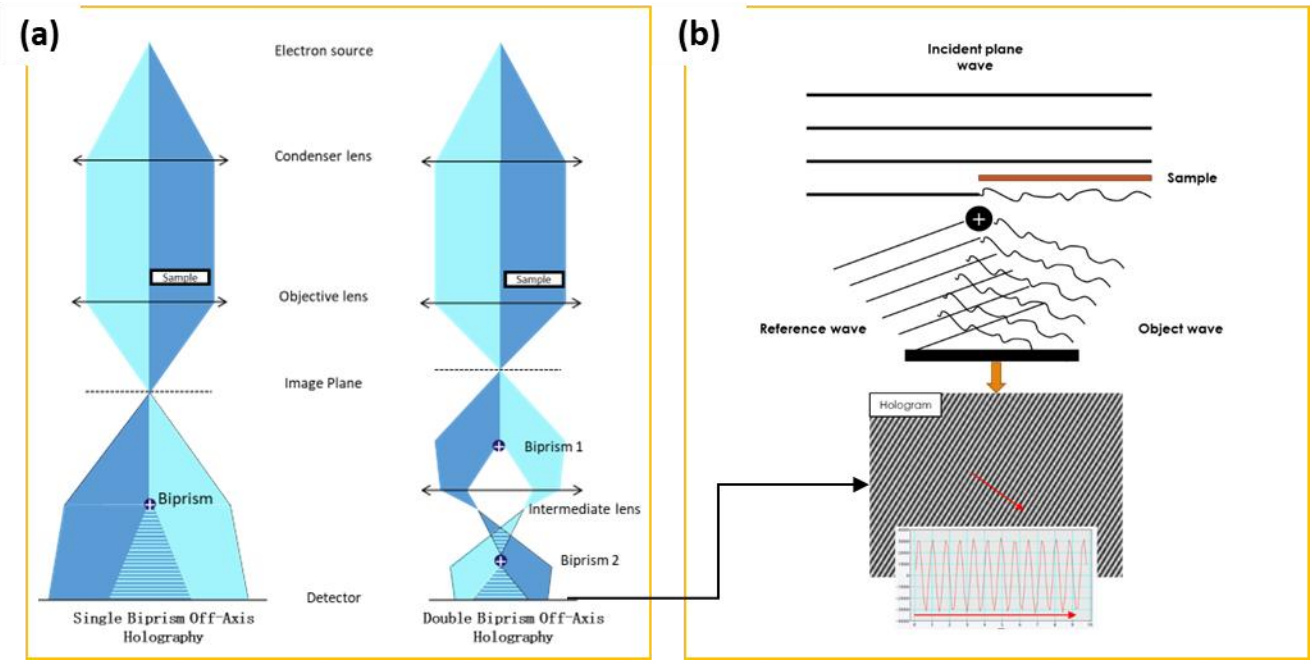

Figure 1. Overview of the off-axis set-up and principle. (a) Ray diagrams of the single biprism (left) and double biprisms (right) off-axis electron holography set-ups. (b) Representation of the interference phenomenon between the unchanged reference wave and the modified object wave generating the black and white fringes. The interference pattern is called the hologram.

The phase sensitivity depends on the electron dose used for the EH experiment (Lichte, 2013, Hÿtch et al., 2021): the higher the dose the better the phase sensitivity, which obviously is lower for studying

electron sensitive materials. In addition, the spatial resolution and the phase sensitivity depend on the size of the mask used for the inverse Fourier transform calculation (supplementary text S1): the larger the mask the higher the spatial resolution but the noisier the resulting phase image. With the I2TEM dedicated microscope, we achieved a maximum phase sensitivity of ~2 mrad at a resolution of 2 nm for holograms obtained in vacuum with a typical electron dose of several thousand $e^-/Å^2$. Such performance cannot be achieved on biological samples which will not support such high doses. The aim on the paper is to demonstrate that electron holography can however provide valuable information on biological materials that classical cryo-TEM cannot. To our knowledge, very few off-axis electron holography results were published on biological samples, with most dating from 2007 and before (Simon et al., 2008) and only one report on cryogenic electron off-axis holography carried out on ferritin (Harscher, 1999) with rather low-resolution images. In this ferritin experiment, the contrast mainly comes from the iron rich core of ferritin that can accommodate up to 4500 Fe^{3+} ions (Moreira et al., 2020). In addition to the less performant hardware in the 2000's, many problems stood against developing electron holography. Among them, at cryogenic temperatures, the increase of inelastic scattering due to the ice layer as well as ice charging reduce the interference fringes contrast and induce local phase shift variations (Glaeser, 2013; Simon et al., 2008).

This paper presents the advancements of RT and cryogenic temperature off-axis electron holography experiments performed on two bacteriophages, or "phages" for short, T4 and T5, which are well-known viruses that specifically infect the *Escherichia Coli* bacteria, their only host (Linares et al., 2023; Yap and Rossmann, 2014). We show an improved contrast of the phase images acquired at high and low electron doses compared to conventional room-temperature TEM images. More interesting, we also provide insights and analysis on the phase shift variations associated either with charge changes within the capsid or with structural remodeling of the T4 tail. Comparison is made with holography performed on the Tobacco Mosaic Virus (TMV) .

3. Material and methods

Preparation of T4 bacteriophages: 5 mL of Escherichia coli MC4100 bacteria (E. coli) obtained from Pierre Genevaux (LMGM-CBI, Toulouse) were first incubated in Lysogeny broth (LB) medium overnight at 37 °C with 180 rpm shaking. The culture was then diluted 10 times and incubated at 37°C with 180 rpm shaking for 30 minutes before adding 450 µL of T4 bacteriophage solution. The mix was incubated for 3.5 hours in the same conditions as previously. Intact and fragmented E. coli were all collected by low-speed centrifugation at 5000 g for 20 minutes at 4 °C. The supernatant containing the bacteriophages was then transferred to a new tube. The obtained solution was then ultra-centrifuged at 35000 g for 40 minutes at 4 °C to pellet the bacteriophages. The LB supernatant was eliminated, and the bacteriophages were resuspended in 10 mL of 10 mM HEPES buffer, pH 7.0 (without additional salts). The solutions were stored at 4°C.

Preparation of T5 bacteriophages: T5st(0) (Genbank Acc AY692264) a heat-stable T5 mutant often used in T5 studies (Barberi et al., 2021; Zivanovic et al., 2014) was produced in the bacterial strain E. coli Fsuβ+, concentrated by NaCl/PEG-induced precipitation, and purified on CsCl gradient as described by Boulanger et al. (Boulanger et al., 1996). Phages were extensively dialyzed against 100 mM NaCl, 10 mM Tris-HCl, pH 7.6, 1 mM CaCl2, and 1 mM MgCl2 at a concentration of 1.8×10^{13} pfu/ml

Tobacco mosaic virus (TMV): TMV was a generous gift from Gérard Péhau-Arnaudet (Institut Pasteur, Paris)

Room temperature TEM grids preparation: 4 µL of the bacteriophage solution was mixed with 1µL of 10 nm gold beads 1/20 (BBI Solutions). 4µL of the mix was drop cast on either a glow-discharged ultrathin carbon grid (Ted Pella ©) or a graphene-quantifoil grid (Sara Bals, EMAT, Belgium). For deposition on the graphene grid, we followed a protocol proposed by Adrian Pedrazo Tardajo (EMAT, Belgium). A plastic ruler (or a plastic sheet) was electrostatically charged and held over the grid while a drop of the phage solution was deposited on the grid. After waiting for 2 minutes, the liquid excess was eliminated, and the ruler removed.

Cryo-EM grids preparation: 4 µL of the bacteriophage solution were mixed with 1µL of 10 nm gold beads diluted 1/20 of the original solution (BBI Solutions). 3 µL of the mix was deposited on a freshly glow-discharged lacey copper grid using a Pelco Easy Glow system operating at 25 mA for 30 sec. The grid was blotted, then plunged in liquid ethane on a Leica EM-GP automated cryo-plunging machine to form vitrified ice.

Calculation of the mass density of the T4 tail: The tail of the T4 bacteriophage is 92.5 nm long and is composed of two coaxial tubes. The inner tube is made of hexameric rings of gp19, while the surrounding tail sheath is composed of hexameric rings of gp18. Each hexamer of gp18 wraps around one hexamer of gp19, which forms a 4.06 nm-high ring (Aksyuk et al., 2009), each ring being rotated by 17.2° relative to the neighboring ones (Yap and Rossmann 2014). Given the molecular weight of gp18 (54.8 kDa) and gp19 (18.4 kDa), the mass density of the extended T4 tail can therefore be estimated as follows: (54.8 + 18.4) x 6 / 4.06 = 108 kDa/nm. When contracted, the inner tube keeps the same configuration with six gp19 molecules making 4.06 nm-high rings, leading to a mass density of 18.4 x 6 / 4,06 = 27 kDa/nm. In contrast, the tail sheath retracts following a conformational change of the gp18 proteins and the 23 rings of gp18 form a 42 nm-long contracted tail (Leiman et al., Cell 2004). The density of the contracted tail sheath can then be calculated as follows: 54.6 x 6 x 23 kDa / 42 nm = 179 kDa/nm. The total density of the retracted tail (retracted sheath + inner tube) therefore equals 206 kDa/nm.

3. Results

The T4 and T5 bacteriophages consist in three main parts (Suppl Figure S1): an icosahedral head or capsid (prolate for T4, isometric for T5) that containing the phage DNA, the tail and the baseplate. Tail fibres are attached to the baseplate and play a role in host cell recognition (Hyman and van Raaij, 2018). Upon infection of bacteria, the T4 tail sheath contracts to allow DNA ejection. Contrary to T4, the T5 bacteriophage's tail is flexible and non-contractile (Arnaud et al., 2017). Although longer, its diameter is twice smaller (12 nm) than that of the T4 tail (24 nm), which make it more challenging to observe.

Experiments were performed on a TEM dedicated to *in-situ* and electron holography experiments (see suppl. Text S2). First experiments were performed with a One View CMOS camera by Gatan©, which was later upgraded by a K3 DDD by Gatan©. As already demonstrated with a K2 camera, using a DDD significantly improves the fringe contrast and subsequently reduces the phase error in off-axis electron holography (Chang et al., 2016). The K3 camera, which has faster readout and improved processing speed (Eisenstein et al., 2019), enabled significant improvements upon the results. At relatively low electron dose (< 80 $e^-/Å^2$), the One View CMOS with scintillator allowed achieving low contrasted interference fringes with a measured contrast less than 10% leading to phase noise higher than 0.1 rad. Under the same conditions, the measured contrast on the K3 camera was about 40%. At higher electron doses, between 80 and 450 $e^-/Å^2$, the measured fringe contrast was above 10% with the One View camera (fringe spacing: ~0.8 nm) and about 45-50% contrast with the K3 (fringe spacing: ~0.6 nm), leading to an estimated 3 to 4 times improvement of the fringe contrast, and therefore a similar decrease in the phase noise.

Off-axis electron holography of unstained bacteriophages at room temperature

Off-axis electron holography was first performed at usual electron doses for these experiments. Figure 2a presents the amplitude and raw phase images calculated from an off-axis hologram acquired on the unstained T4 bacteriophage. The hologram was recorded over 40 seconds under constant live drift correction, and the π-shift mid-acquisition process was activated. The total electron dose was 484 $e^-/Å^2$, which is a high dose for a biological specimen. However, we observed that the general morphology of the phages remained intact at this dose.

The amplitude image (Figure 2a, left), which corresponds to an in-focus zero-loss energy-filtered BF image (Yesibolati et al., 2020), displayed a low-contrast phage with no morphological detail of the capsid and barely visible tails. The phase image in Figure 2a (right) showed a higher contrast in addition to the detection of the tails. The capsid appeared rounded, contrary to its native icosahedral shape, which was likely due to sample dehydration. The phase sensitivity, measured on the low contrast graphene support, was 0.05 rad at a spatial resolution of 1 nm. The mean phase shift, as shown in the phase profile in Figure 2b is 2.7 rad (taking into account the background signal). In general, the average phase shift measured across the 40-50 capsids in our entire data set was 2.5 ±0.3 rad, and 0.25 ±0.05 rad on non-contracted tails, similar to the presented phase image. On the hologram of a contracted T4 phage acquired (suppl. Figure S2), we measured a higher phase shift of 0.9 rad compared to a non-contracted tail due to the thickness increase and the structural change of the tail sheath upon contraction (Aksyuk et al., 2009).

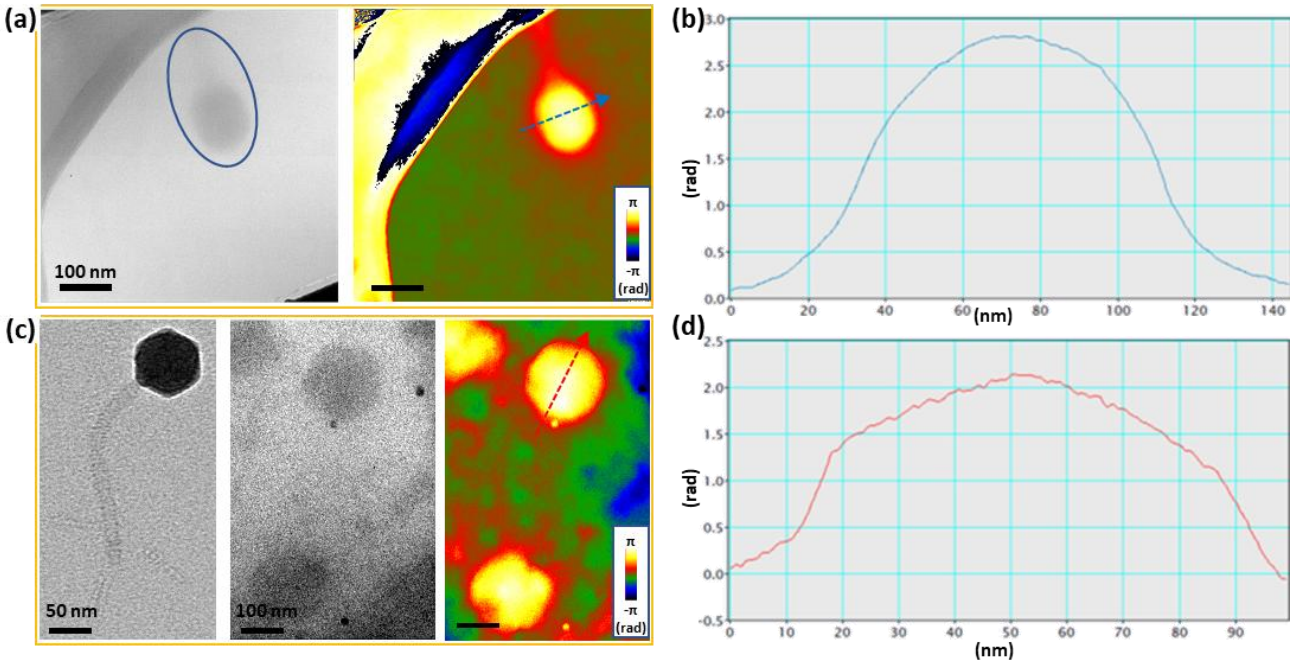

Figure 2. High electron dose RT off-axis electron holography experiment on the T4 (a-b) and T5 (b-c) bacteriophages. (a) T4 amplitude (left) and raw phase (right) images of the analysed hologram. (b) Phase profile of the T4 capsid shown in (a) represented by the blue arrow. (c) Positively stained T5 phage (left) acquired on a Jeol 1400. T5 amplitude (middle) and phase (right) images. (d) Phase profile of the capsid shown in (c) represented by the red arrow.

Off-axis holograms were also acquired on T5 bacteriophages at similar electron doses (Figure 2c). Unlike with T4, the thinner tail in T5 virions that can be seen in the positively stained T5 (Figure 2c left) was not detected, in neither the amplitude (Figure 2c middle) nor the phase (Figure 2c right) images, suggesting a higher sensitivity to electron beam irradiation. In this example, we measured a phase shift of 2.1 rad at the capsid (Figure 2d) while with a phase sensitivity of 0.05 rad, consistent with the value

measured on T4 particles, and a spatial resolution of 1.6 nm. The average phase shift value measured on 30 capsids was 2.5 rad.

These high-dose electron holography experiments performed on unstained bacteriophages provided high sensitivity phase images with low phase noise and of much higher contrast compared to under-focused BF images. However, the spatial resolution of these images did not match that of negatively stained samples in BF microscopy (see Suppl. Figure S3 for T4 phage comparison with other microscopy methods), as shown by the lack of details on the T4 tail, or even the absence of phase contrast on the T5 tail. We attributed this lack of resolution to the electron beam damages resulting of the high dose irradiation in absence of protection by a contrasting agent.

Implementing low-dose off-axis electron holography at room temperature

To limit radiation damages on the sample, we implemented a low-dose workflow on the I2TEM microscope (see suppl. text S2 and S3 and suppl. Figure S4) by developing the plugin 'Lenses-BD' to save two sets of lenses parameters configurations: 'search mode' at low magnification to select the field of view, and 'record mode' for high magnification hologram recording (see suppl. Figure S5).

Examples of phase images of T4 and T5 bacteriophages extracted from low-dose RT holograms are displayed in Figure 3. For the T4 virion displayed in Figure 3a, the electron dose was 30 $e^-/Å^2$ for a 10 second exposure without π-shifting, resulting in a phase image of 0.08 rad phase sensitivity and a spatial resolution of the phase image equal to 2.9 nm. The capsid induced a 2.6 rad maximum phase shift (Fig. 3b) and the tail, less visible than at higher dose, a 0.25 rad phase shift. The amplitudes of these phase shifts are similar to the one measured at high-dose and attest the uncorrelation of the phase shift with the electron dose.

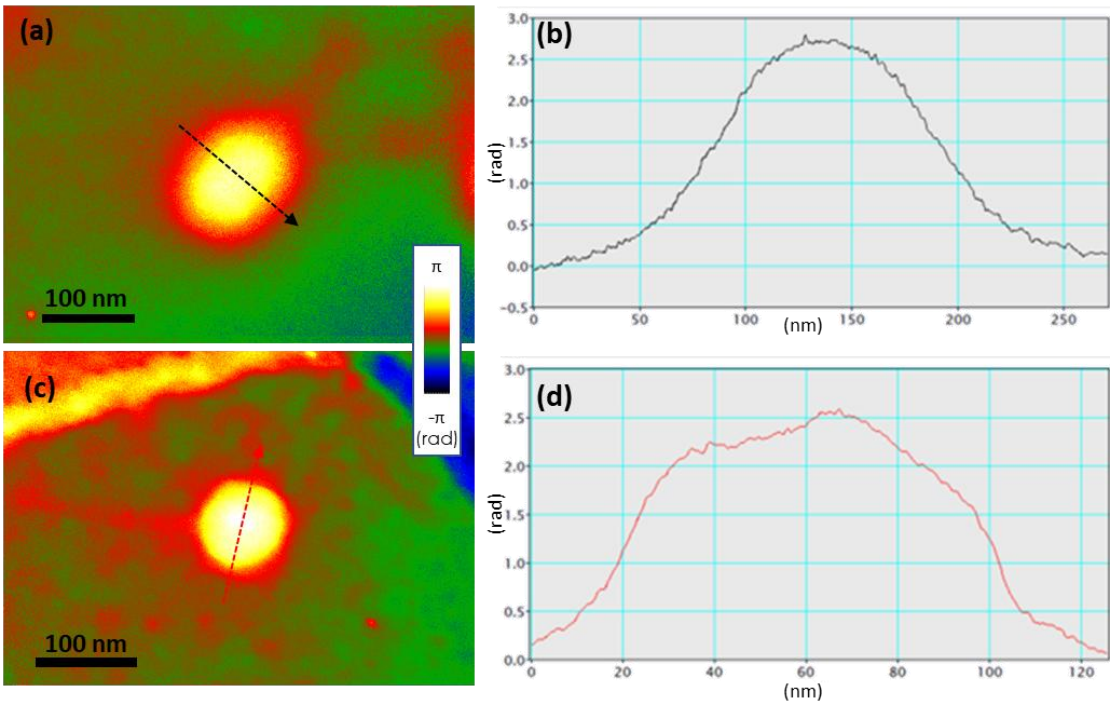

Figure 3. Low electron dose RT off-axis electron holography. (a) Phase image of the T4 bacteriophage. (b) Phase profile drawn across the T4 phage in (a) and shown by the black arrow. (c) Phase image of the T5 bacteriophage. (d) Phase profile drawn across the T5 phage in (c) and shown by the orange arrow.

The T5 phage in Figure 3c was observed with a total dose of 60 $e^-/Å^2$, leading to a phase sensitivity of 0.06 rad (~$2\pi/100$) at a spatial resolution of 1 nm. The tail was visible, unlike at high dose, but not the details of the tail rings. The head (DNA filled capsid) induced a phase shift of 2.5 rad (Figure. 3d), a value similar to the T4 bacteriophage capsid, while the phase shift was of 0.25 rad for the tail.

These experiments show that it is possible to obtain contrast for biological specimen in these phase images under low-dose conditions, while these samples are barely visible in bright field mode in the same condition. As expected, this is paralleled by a better structural preservation of the sample from radiation damages. However, the increased phase noise resulting from the low electron dose prevented the observation of structural features like the 4-nm periodic stacking of the tail rings, despite the use of a highly sensitive DDD camera.

Cryogenic off-axis electron holography of vitrified T4 and T5 bacteriophages

In order to further improve structural preservation of the sample from the electron beam and image the phages in their native hydrated state, we turned to cryogenic TEM. Phages were embedded in vitreous ice by plunge-freezing in liquid ethane and observed with a liquid nitrogen-cooled holder, which preserves to some extent the structure of the sample from the electron beam (Glaeser and Taylor, 1978). We first assessed beam-induced damages on vitrified bacteriophages on a Jeol 2100 LaB_6 200 keV TEM equipped with a Gatan Ultrascan US4000 (4kx4k) CCD and a Gatan Imaging Filter (GIF Quantum model 964) (Schröder et al., 1990). A selected ROI was increasingly irradiated with multiple exposures of equal doses. Beam-induced damages were assessed both qualitatively and by a cross-correlation with the first image using the 'image J' software (Suppl. Figure S6). The electron doses in these experiments are measured with ± 10 $e^-/Å^2$ uncertainty (each image is obtained using a 20 $e^-/Å^2$ exposure). The main observations were the following: (1) the tail structure was damaged at doses around 70 $e^-/Å^2$, while the phage overall shape remained qualitatively intact at this dose; (2) the capsid decoration protein Hoc was damaged (loss of contrast) around 90 $e^-/Å^2$; (3) the capsid structure was damaged and bubbles formed in the ice at doses around 110 $e^-/Å^2$.

Off-axis holography of vitrified T4 phages was then performed on the I2TEM at cryogenic temperature for 20 seconds with the π-shift procedure and a total dose of 50 $e^-/Å^2$, that is below 70 $e^-/Å^2$ at which radiation damages are detected. The amplitude and phase images of a such an experiment are displayed in Figures 4a and 4b. As expected at this low electron dose, the T4 capsids were barely visible in the amplitude image and tails were not detected. Under a high contrast lens microscope (Jeol 2100 HC), the tail becomes slightly visible in an in-focus BF image, with a low contrast and a barely visible if not at all, baseplate. (Suppl. Figure S3f). In contrast, the phase image fully revealed the bacteriophage structure including the capsid, the tail, as well as the thinner neck linking the capsid and tail. Importantly, the capsids appeared with their icosahedral shape, and the baseplates were clearly detected unlike in room temperature experiments. The rings of the phage tails were nonetheless not visible. In this experiment, the phase shift measured at the capsid at cryogenic temperature was 0.85 rad maximum, lower than the 2.5 rad measured at RT. The high noise (phase sensitivity = 0.16 rad at a spatial resolution of 1.3 nm) appeared to be due the ice thickness variations, which induce phase variations as seen on the right side of the phase image in Figure 4b, as well as the ice overlap with our object as no vacuum exists around the sample.

Similar cryogenic electron holography experiments were carried out on T5 bacteriophages at 50 $e^-/Å^2$ (Figure 4 c-f). The phase sensitivity was 0.08 rad, a better value which we ascribe to a thinner ice and a buffer solution with a composition. The spatial resolution of the phase images, was fixed for all cryo-EM experiments by adjusting the biprism voltages, leading to the target interfringe value of 1.3 nm. As

observed with T4 virions, the T5 structure was well preserved with the capsid shape and the thin tail contrasted and identifiable. The baseplate, located at the end of the tail, is not well defined. Similarly to T4, full capsids (Figure 4d) displayed a maximum phase shift of 0.95 rad at cryogenic temperature (Figure 4f), a much lower value than at RT (2.5 rad). Interestingly, an empty capsid (Figure 4e) induced almost no phase shift in its center and about 0.2-0.3 rad at its periphery (Figure 4f), indicating that the phase shift measured in full capsid is mostly due to its content rather than the empty shell.

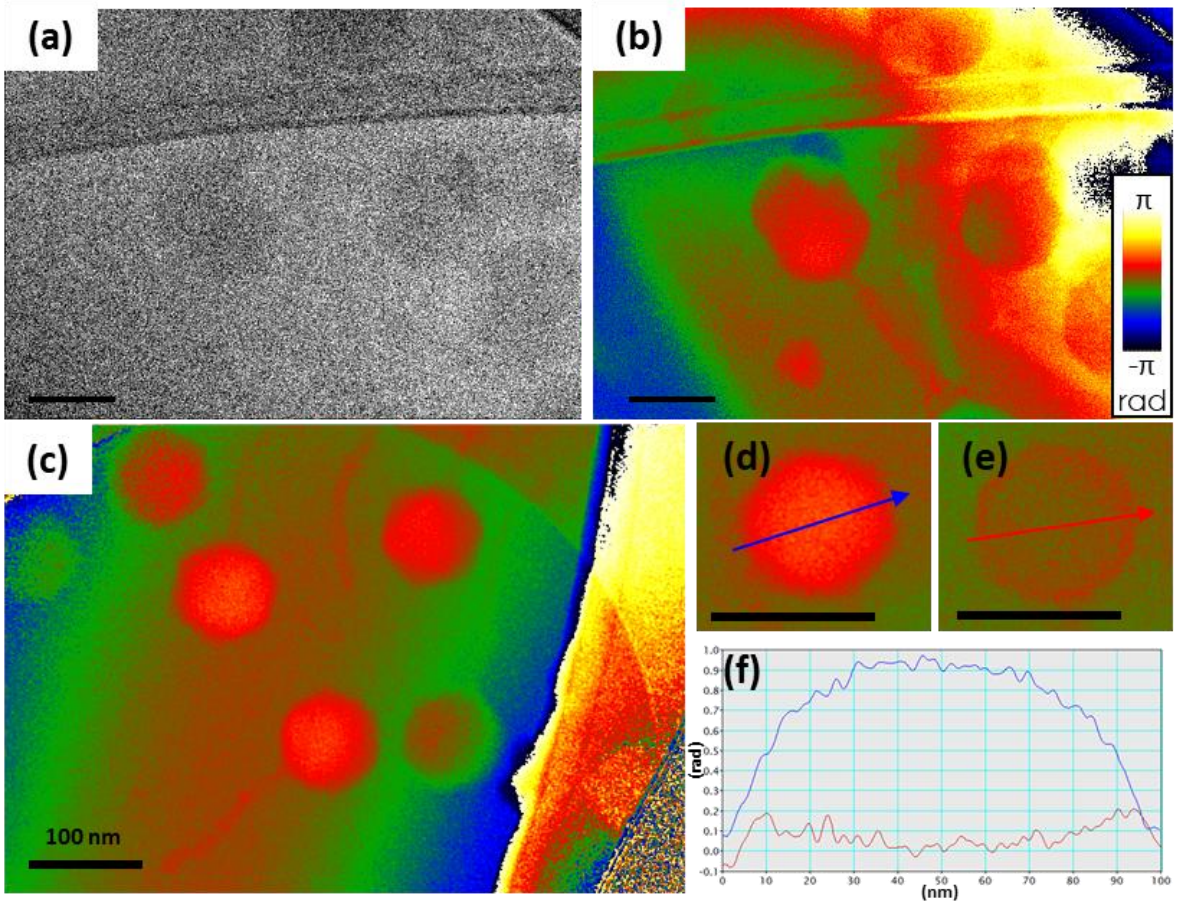

Figure 4. Cryogenic off-axis holography. (a-b) Low electron dose cryogenic off-axis holography of vitrified T4 phages. (a) Amplitude image. (b) Phase image. (c-f) Low electron dose cryogenic off-axis holography of vitrified T5 phages. (c) Phase image. (d) Phase image (cryo) of a full T5 bacteriophage head. (e) Phase image (cryo) of an empty T5 bacteriophage head. (f) Phase profile of the full head (blue profile) and the empty head (red profile) in (d) and (e).

These data on T4 and T5 phages show the higher capabilities of cryogenic off-axis electron holography to observe the structure of biological samples when compared to similar experiments at room temperature, but also point to a loss of phase sensitivity. Indeed, the phase shift measured at the capsid location is substantially reduced by the presence of the ice compared to phase shift measured on the sample only lying on the graphene support used at RT (see the detailed explanation in suppl. Text S4 and Suppl. Figure S7). In addition to this extrinsic phase shift decay, the MIP of the capsid and its contents also decreases with decreasing temperature due to the higher density of biological material at low temperature: this point was demonstrated by M.N. Yesibolati et al. in (Yesibolati et al., 2020), by measuring by off-axis electron holography the MIP of water of about 4.48 eV in the liquid state compared to 3.5 eV measured in vitreous ice (Harscher and Lichte, 1998). Therefore, thinness of the ice, which is known as a major optimization parameter for bright field imaging of biological molecules by cryo-EM,

may be even more critical in the case of cryogenic electron holography.

As expected, phase sensitivity in cryogenic conditions improved when holography on T4 or T5 phages was performed with higher electron doses, going from 0.16 to 0.07 rad for doses increasing from ~30 to 100 $e^-/Å^2$ (Figure 5a). However, some experiments did show good phase sensitivity (0.07 rad) at low dose, most probably due to more homogeneous and thinner ice. The sensitivity threshold required to detect structural features of about 4 nm size (i.e. the stacking periodicity of the rings in the T4 tail) was estimated

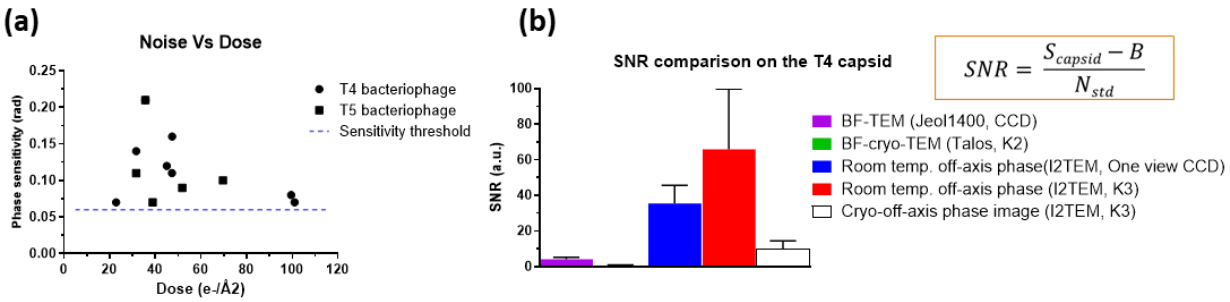

to be around 0.06 rad, which may explain why we are not able to observe the tail rings.

Figure 5. Noise and SNR evaluation of the off-axis holography results. (a) Phase sensitivity in radians of the T4 and T5 phase images obtained by cryo-off-axis holography plotted in function of the electron dose. The sensitivity threshold of 0.06 rad, which is shown with the blue dotted line, is our estimation for visualizing the tail rings. (b) Histogram comparing the best achievable SNR using different TEM techniques. Every histogram is the average of three values, and the error bar corresponds to the standard deviation. The SNR formula is displayed with S_{capsid} the capsid mean signal, B the background mean signal, and N_{std} the noise (standard deviation).

Finally, the performance of cryogenic off-axis electron holography was also assessed by calculating the signal-to-noise ratio (SNR) of TEM images obtained at room temperature and in cryo conditions, in bright field or holography, with different detectors (Figure 5b). Bright field electron microscopy at room temperature was performed on a 120keV TEM using a CCD camera, while images in cryogenic conditions were acquired on a 200 keV Thermofisher© Talos Arctica microscope equipped with a K2 DDD. SNR was calculated using the following formula:

$$SNR = \frac{S_{capsid} - B}{N_{std}}$$

with:

- S_{capsid} the average signal measured inside the capsid.
- B the average background signal (to correct for errors due to the support around the phage not being at zero) measured in an empty and flat area.
- N_{std} is the standard deviation of the average signal of the background (noise).

Phase images obtained by high-dose off-axis holography at room temperature showed significant SNR improvements by almost one order of magnitude when compared to bright field. The SNR average value rose from 4.1 in bright field mode at 80 KeV on a CDD camera to 35.5 by holography using a CMOS detector, and this value almost doubled to 65.9 when adding the benefit of a DDD. Importantly, despite increased phase noise due to the amorphous ice, phase images obtained by off-axis holography in the I2TEM also improved the SNR very substantially in cryogenic conditions, from 0.8 to 8.5, when compared to bright field images acquired on the Talos Arctica, using a DDD on both microscopes.

Dependence of phase shift on electric charges within the capsid

As indicated in the introduction, the phase shift experienced by the electron beam depends on the local electrostatic potential. This property has been used to probe the electrostatic potential both due to the mean inner potential (MIP) of the material under study and possible additional electrostatic fields due to free electric charges. Our experiments show that a much higher phase signal in the head relative to the tail, and a striking difference between full and empty capsids. We therefore wondered whether part of this phase shift reflected the electrostatic potential due to the negative charge of DNA.

It has been shown that ions can diffuse through the T5 bacteriophage capsid wall and modify the global charge of the particle (Cordova et al., 2003). Hence, the tetravalent cation spermine is thus able to neutralize the otherwise negatively charged DNA (Raspaud et al., 1999; Yamasaki et al., 2001), resulting in small DNA rearrangements within the capsid, without any DNA ejection or major shape, size and conformational changes of the capsid (Frutos et al., 2016). We therefore investigated the capability of electron holography to detect charge variations induced by spermine addition to the T5 bacteriophage suspension, and compared phase images obtained at RT on non-treated and spermine-treated T5 phages. We performed these comparative experiments on multiple T5 samples and observed a significant phase shift decay from 2.5 rad for the non-treated phages to 1.5 rad for the spermine-treated ones as shown in the Figure 6. This experiment demonstrates that electron holography is able to probe local electrostatic potential changes due to local electric charges resulting here from interaction between DNA molecules and counterions.

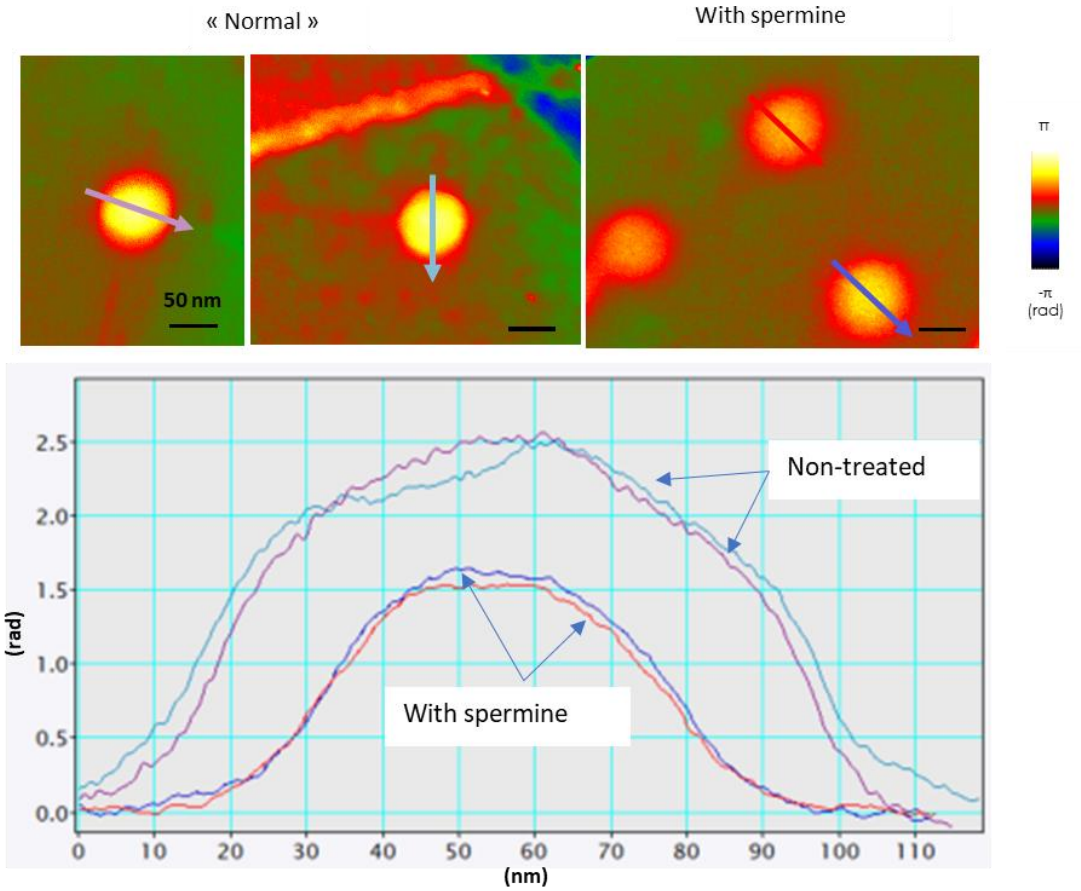

Figure 6. Phase shift variation with charge at RT. High electron dose RT phase image of non-treated T5 top (left and middle), and spermine-treated T5 (top right). Below: Phase profile of non-treated and spermine-treated T5 (arrows shown in the upper images).

Similar observations of the electric charges effect can be seen in the phase images in Figures. 2a, 2c, 3a and 3c, and in Figure. 6 of the non-treated sample. In these phase images, the "yellow" areas of about 85 nm large with phase shift larger than 1.5 rad correspond to the DNA-filled capsid itself, while the "red" areas which extend over few tens of nanometers away from the capsids with phase shift decreasing with the distance to the capsid from about 1.5 rad to 0 correspond to the electrostatic fields resulting of the electrostatic charges of DNA located within the capsid. As observed in phase shift image of the spermine-treated sample (Figure. 6 right) the electrostatic fields due to the less charged capsid is evidently lower and extends to 0 over a smaller distance. This local charge variation detection offers a new potential application for off-axis holography in the absence of current charge measuring techniques at the level of single objects.

Relationship between material structure and electrostatic phase shift

In inorganic compounds of single type of atom (Si, Al...), the MIP can be deduced from its structure and density. However, it necessitates considering the material electronic structure - even different forms of graphite have different MIP (Auslender et al. 2021). In contrast, establishing a link between the MIP and the density in biological materials is by far more difficult as the latter are composed of many more different types of atoms with various electronic structures and their MIP depends on the sample environment.

To explore this question, we compared the phase shift values in the two configurations of the T4 phage tail with the mass density of these two structural states, when it is extended or contracted (Suppl. Figures S1 and S2). As described in Material and methods, we estimated the mass density of the T4 tail to 108 kDa/nm in the extended form, while this value increases to 206 kDa/nm upon contraction of the tail sheath. We compared these values to the electrostatic phase shift measured from phase images on profiles perpendicular to the tails, namely 0.25 rad for the extended conformation and 0.8 rad for the contracted form. As shown in Table I, the ratio of the electrostatic phase shift to the sample thickness $\frac{\varphi(x,y)}{t}$ was almost proportional to the mass density, which could be explained as both consist of the same molecules but being in different configuration (the diameter of the extended and contracted tail is 24 and 33 nm respectively, however, the thickness of the material contributing to the electrostatic phase shift is 19 nm and 28 nm, respectively, when removing the 5 nm-wide lumen of the empty inner tube). In that case, the increase of the relative phase shift / thickness can be related partly to the increased density but also to the change of the electronic structure.

We next performed EH on the well-characterized Tobacco mosaic virus (TMV) (Sachse et al. 2007), whose mass density is estimated to 131 kDa/nm (see TEM holograms in Suppl. Figure S9). TMV is a rod-shaped plant virus with a typical length of 300 nm, a diameter of 18 nm and a ~4 nm-wide central channel that contains genomic RNA. Electrostatic phase profiles extracted perpendicular to the TMV main axis indicated a mean value of the electrostatic phase shift measured of 0.47 rad. In this case, the ratio [$\frac{\varphi(x,y)}{t}$ / mass density] was ~1.5 higher than for the T4 samples. This higher MIP likely reflects the difference in the structure and the charge of the TMV when compared to the T4 tail, like the presence of phosphates in the genomic RNA packed in the TMV capsid.

	Electrostatic phase shift - $\varphi(x,y)$	sample thickness (t)	$\frac{\varphi(x,y)}{t}$	density	$\frac{\varphi(x,y)}{t}$ / density
TMV	0.47 rad	18 nm	0.026	131 kDa/nm	1.98 E-4
T4 Phage extended tail	0.25 rad	19 nm	0.013	108 kDa/nm	1.2 E-4
T4 Phage contracted tail	0.8 rad	28 nm	0.028	206 kDa/nm	1.35 E-4

Table I

4. Discussion

In this article, we showed significant improvements on the contrast of images using off-axis electron holography experiments performed on unstained biological samples. This was done at both RT and cryogenic temperature as well as high and low electron doses. In cryo, the phase noise associated to the required low-dose is added to the decay of the SNR due to the interferometric overlap of ice areas in the off-axis holography experiment. Regardless, we were able to obtain preliminary results, with phase images showing the detailed bacteriophages morphology, setting a new checkpoint in contrast-enhanced imaging of biological methods. More work is however needed to reduce the phase noise and special care has to be given to prepare the cleanest possible sample solution (no contaminations) deposited on flat and thin support (as graphene layer succeed to be) and thin ice layer of constant thickness for cryogenic experiments. Beside inherent requirements of working in low dose conditions at cryogenic temperatures

on samples embedded in vitreous ice, another limitation in cryogenic off-axis holography experiments comes from the absence of dedicated automated TEM allowing to combine cryo-EM and off-axis electron holography. In particular, the I2TEM microscope is dedicated to material sciences without optimized tools for low dose experiments. Despite the current limitations, spatial resolution can be improved if the fringe spacing is reduced (by increasing the biprism voltage) while maintaining a sufficient signal-to-noise ratio (SNR), i.e., sufficient fringe contrast. One possibility would be to create vacuum holes near the regions of interest (ROIs) so that the reference beam passing through them does not experience additional phase shift or intensity loss and thus reduce noise in the phase image. Cryo FIB milling (Rigort and Plitzko, 2015) could be used to create such holes near the ROI. This could allow resolving features up to the maximum spatial resolution defined by the fringe spacing while maintaining sufficient phase sensitivity and finding the right compromise between a smaller fringe spacing and a sufficiently large field of view. However, for the bacteriophage samples, the spatial resolution we achieved was more than sufficient to resolve the details we wanted to study.

We also demonstrated that the DNA neutralization of the T5 capsid by spermine affected the measured maximum phase shift as the capsid became less negatively charged. Quantifying the capsid charges variation would require to perform electron off-axis experiment of sample almost "floating" in vacuum and not lying on a conducting support (Gatel et al., 2013). Free charges located on the support could indeed partially screen the electric potential of the capsid and lead to artifacts in the charge measurement. Quantifying the charges also requires to separate, in the electrostatic potential $V(x, y, z)$ of equation (1), the contribution of the MIP from that of these additional charges. The MIP depends on several factors related to the electronic structure of the sample. The number of these factors increases with the number of components of the studied sample.

For a given sample, EH can give relevant information on the structural modifications (electronic structure, density, etc.) resulting from configuration changes.

The MIP depends on several factors related to the electronic structure of the sample. The number of these factors increases with the number of components of the studied sample and is not straightforward for biological samples. As suggested by the comparison of the electrostatic phase shift for the T4 tail, EH may give relevant information on the structural modifications (electronic structure, density, etc.) resulting from configuration changes. In contrast, drawing information from samples with different composition and structure may be more complicated, as illustrated here by our comparison of T4 and TMV particles. We believe that semi-quantitative methods could be developed for such complex specimens, while quantitative measurements could be done on simpler models like small proteins with known 3D structures with the help of simulations as comparisons.

5. Conclusion

The ability of off-axis holography to detect charge variations within biological objects could be ground-breaking, as no method for local charge measurement currently exist for biological sample. In addition, for a given sample, EH is able to give relevant information on the structural modifications (electronic structure, density, etc.) resulting from configuration change. Further developing off-axis holography, as well as combining it with other methods like in-line electron holography could further push the limits of this technique and enable the achievement of even better and more reliable results.

Declaration of competing interest

The authors declare that they have no known competing financial interests or personal relationships that could have appeared to influence the work reported in this paper.

Acknowledgments and funding statement

The authors are thankful to Pierre GENEVAUX for providing us with the T4 phages, to Prof. Sara BALS and Adrian PEDRAZO TARDAJO from the EMAT laboratory in Antwerp, Belgium for providing us with graphene-quantifoil TEM grids, as well as Cécile Marcelot for helping with the I2TEM experiments. We also acknowledge the METi imaging facility, member of TRI-Genotoul and of the national infrastructure France-BioImaging supported by the French National Research Agency (ANR-10-INBS-04). This work was carried out as part of a doctoral thesis funded by the Region Occitanie (France) and the University of Toulouse as part of the "CryHolo" project. The work was financially supported by the MITI of the CNRS through the project "CryHolo".

References

Aksyuk, A.A., Leiman, P.G., Kurochkina, L.P., Shneider, M.M., Kostyuchenko, V.A., Mesyanzhinov, V.V., Rossmann, M.G., 2009. The tail sheath structure of bacteriophage T4: a molecular machine for infecting bacteria. The EMBO Journal 28, 821–829. https://doi.org/10.1038/EMBOJ.2009.36

Andersen, I.M., Rodríguez, L.A., Bran, C., Marcelot, C., Joulie, S., Hungria, T., Vazquez, M., Gatel, C., Snoeck, E., 2020. Exotic Transverse-Vortex Magnetic Configurations in CoNi Nanowires. ACS Nano 14, 1399–1405. https://doi.org/10.1021/acsnano.9b07448

Arnaud, C.A., Effantin, G., Vivès, C., Engilberge, S., Bacia, M., Boulanger, P., Girard, E., Schoehn, G., Breyton, C., 2017. Bacteriophage T5 tail tube structure suggests a trigger mechanism for Siphoviridae DNA ejection. Nature Communications 8. https://doi.org/10.1038/s41467-017-02049-3

Auslender A., Levi G, Ezersky V, Gorfman S., Dieguez O., Kohn A. Carbon, Vol. 179, p288, 2021 https://doi.org/10.1016/j.carbon.2021.04.019

Barberi, L., Livolant, F., Leforestier, A., Lenz, M., 2021. Local structure of DNA toroids reveals curvature-dependent intermolecular forces. Nucleic Acids Research 49, 3709–3718. https://doi.org/10.1093/nar/gkab197

Benjin, X., Ling, L., 2020. Developments, applications, and prospects of cryo- electron microscopy. Protein Science 29, 872–882. https://doi.org/10.1002/pro.3805

Boulanger, P., Le Maire, M., Bonhivers, M., Dubois, S., Desmadril, M., Letellier, L., 1996. Purification and Structural and Functional Characterization of FhuA, a Transporter of the *Escherichia coli* Outer Membrane. Biochemistry 35, 14216–14224. https://doi.org/10.1021/bi9608673

Brenner, S., Horne, R.W., 1959. A negative staining method for high resolution electron microscopy of viruses. Biochimica et Biophysica Acta 34, 103–110. https://doi.org/10.1016/0006-3002(59)90237-9

Cassidy, C., Dhar, A., Shintake, T., 2017. Determination of the mean inner potential of cadmium telluride via electron holography. Appl. Phys. Lett. 110. https://doi.org/10.1063/1.4981809

Chang, S.L.Y., Dwyer, C., Barthel, J., Boothroyd, C.B., Dunin-Borkowski, R.E., 2016. Performance of a direct detection camera for off-axis electron holography. Ultramicroscopy 161, 90–97. https://doi.org/10.1016/J.ULTRAMIC.2015.09.004

Cordova, A., Deserno, M., Gelbart, W.M., Ben-Shaul, A., 2003. Osmotic Shock and the Strength of Viral Capsids. Biophysical Journal 85, 70–74. https://doi.org/10.1016/S0006-3495(03)74455-5

D'Imprima, E., Kühlbrandt, W., 2021. Current limitations to high-resolution structure determination by single-particle cryoEM. Quart. Rev. Biophys. 54, e4. https://doi.org/10.1017/S0033583521000020

Dubochet, J., McDowall, A.W., 1981. VITRIFICATION OF PURE WATER FOR ELECTRON MICROSCOPY. Journal of Microscopy 124, 3–4. https://doi.org/10.1111/j.1365-2818.1981.tb02483.x

Egerton, R.F., Li, P., Malac, M., 2004. Radiation damage in the TEM and SEM. Micron 35, 399–409. https://doi.org/10.1016/j.micron.2004.02.003

Eisenstein, F., Danev, R., Pilhofer, M., 2019. Improved applicability and robustness of fast cryo-electron tomography data acquisition. Journal of Structural Biology 208, 107. https://doi.org/10.1016/J.JSB.2019.08.006

Frutos, M.D., Leforestier, A., Degrouard, J., Zambrano, N., Wien, F., Boulanger, P., Brasilès, S., Renouard, M., Durand, D., Livolant, F., 2016. Can Changes in Temperature or Ionic Conditions Modify the DNA Organization in the Full Bacteriophage Capsid? J. Phys. Chem. B 120, 5975–5986. https://doi.org/10.1021/acs.jpcb.6b01783

Gabor, D., 1948. A New Microscopic Principle. Nature 161, 777–778. https://doi.org/10.1038/161777a0

Gallagher, J.R., Kim, A.J., Gulati, N.M., Harris, A.K., 2019. Negative-Stain Transmission Electron Microscopy of Molecular Complexes for Image Analysis by 2D Class Averaging. Current Protocols in Microbiology 54. https://doi.org/10.1002/CPMC.90

Gatel, C., Dupuy, J., Houdellier, F., Hÿtch, M.J., 2018. Unlimited acquisition time in electron holography by automated feedback control of transmission electron microscope. Applied Physics Letters 113, 133102. https://doi.org/10.1063/1.5050906

Gatel, C., Lubk, A., Pozzi, G., Snoeck, E., Hÿtch, M., 2013. Counting elementary charges on nanoparticles by electron holography. Physical Review Letters 111. https://doi.org/10.1103/PhysRevLett.111.025501

Glaeser, R.M., 2013. Invited Review Article: Methods for imaging weak-phase objects in electron microscopy. Review of Scientific Instruments 84. https://doi.org/10.1063/1.4830355

Glaeser, R.M., Taylor, K.A., 1978. Radiation damage relative to transmission electron microscopy of biological specimens at low temperature: a review. Journal of Microscopy 112, 127–138. https://doi.org/10.1111/j.1365-2818.1978.tb01160.x

Harada, K., Tonomura, A., Togawa, Y., Akashi, T., Matsuda, T., 2004. Double-biprism electron interferometry. Applied Physics Letters 84, 3229–3231. https://doi.org/10.1063/1.1715155

Harscher, A., 1999. Electron holography of biological objects: basics and examples of applications. Tübingen, Germany.

Harscher, A., Lichte, H., 1998. Inelastic Mean Free Path and Mean Inner Potential of Carbon Foil and Vitrified Ice measured with Electron Holography., in: Electron Microscopy General Interest and Instrumentation. IOP Publishing Ltd, Bristol.

Hÿtch, M., Gatel, C., 2021. Phase detection limits in off-axis electron holography from pixelated detectors: gain variations, geometric distortion and failure of reference-hologram correction. Microscopy 70, 47–58. https://doi.org/10.1093/jmicro/dfaa044

Hytch, M.J., Houdellier, F., Hüe, F., Snoeck, E., 2011. Dark-field electron holography for the measurement of geometric phase. Ultramicroscopy 111, 1328–1337. https://doi.org/10.1016/J.ULTRAMIC.2011.04.008

Kühlbrandt, W., 2014. The Resolution Revolution. Science 343, 1443–1444. https://doi.org/10.1126/science.1251652

Lichte, H., 2013. Electron Holography: Phases matter. Journal of Electron Microscopy 62. https://doi.org/10.1093/jmicro/dft009

Linares, R., Arnaud, C.-A., Effantin, G., Darnault, C., Epalle, N.H., Boeri Erba, E., Schoehn, G., Breyton, C., 2023. Structural basis of bacteriophage T5 infection trigger and *E. coli* cell wall perforation. Sci. Adv. 9, eade9674. https://doi.org/10.1126/sciadv.ade9674

Leiman, Petr G. et al., Cell, Volume 118, Issue 4, 419 - 429 https://doi.org/10.1016/j.cell.2004.07.022

Möllenstedt, G., Düker, H., 1955. Fresnelscher Interferenzversuch mit einem Biprisma für Elektronenwellen. Die Naturwissenschaften 42, 41. https://doi.org/10.1007/BF00621530/METRICS

Moreira, A.C., Mesquita, G., Gomes, M.S., 2020. Ferritin: An Inflammatory Player Keeping Iron at the Core of Pathogen-Host Interactions. Microorganisms 8, 589. https://doi.org/10.3390/microorganisms8040589

Ortiz Ortega, E., Hosseinian, H., Rosales López, M.J., Rodríguez Vera, A., Hosseini, S., 2022. Characterization Techniques for Morphology Analysis. pp. 1–45. https://doi.org/10.1007/978-981-16-9569-8_1

Peankuch, E., Kausche, G.A., 1940. Isolierung und, übermikroskopische Abbildung eines Bakteriophagen. Naturwissenschaften 28, 46–46. https://doi.org/10.1007/BF01486932
Raspaud, E., Chaperon, I., Leforestier, A., Livolant, F., 1999. Spermine-Induced Aggregation of DNA, Nucleosome, and Chromatin. Biophysical Journal 77, 1547–1555. https://doi.org/10.1016/S0006-3495(99)77002-5
Rigort A, Plitzko JM. Cryo-focused-ion-beam applications in structural biology. Arch Biochem Biophys. 2015 Sep 1;581:122-30. doi: 10.1016/j.abb.2015.02.009. Epub 2015 Feb 20. PMID: 25703192.
Ruska, H., 1940. Die Sichtbarmachung der bakteriophagen Lyse im Übermikroskop. Die Naturwissenschaften 28, 45–46. https://doi.org/10.1007/BF01486931/METRICS
Sachse C., Chen J.-Z., Coureux P.-D., Stroupe M. E., Fändrich M., Grigorieff N., Journal of Molecular Biology, Volume 371, Issue 3, 2007, Pages 812-835 https://doi.org/10.1016/j.jmb.2007.05.088
Scheres, S.H.W., 2012. A Bayesian View on Cryo-EM Structure Determination. Journal of Molecular Biology 415, 406. https://doi.org/10.1016/J.JMB.2011.11.010
Schröder, R.R., Hofmann, W., Ménétret, J.F., 1990. Zero-loss energy filtering as improved imaging mode in cryoelectronmicroscopy of frozen-hydrated specimens. Journal of Structural Biology 105, 28–34. https://doi.org/10.1016/1047-8477(90)90095-T
Simon, P., Lichte, H., Formanek, P., Lehmann, M., Huhle, R., Carrillo-Cabrera, W., Harscher, A., Ehrlich, H., 2008. Electron holography of biological samples. Micron 39, 229–256. https://doi.org/10.1016/j.micron.2006.11.012
Singer, A., Sigworth, F.J., 2020. Computational Methods for Single-Particle Electron Cryomicroscopy. Annual Review of Biomedical Data Science 3, 163–190. https://doi.org/10.1146/annurev-biodatasci-021020-093826
The Nobel Prize in Chemistry 2017 NobelPrize.org. Nobel Prize Outreach AB 2024. Thu. 19 Dec 2024. https://www.nobelprize.org/prizes/chemistry/2017/summary/
Tonomura, A., 1998. The Quantum World Unveiled by Electron Waves, The Quantum World Unveiled by Electron Waves. WORLD SCIENTIFIC. https://doi.org/10.1142/2976
Voelkl, E., Tang, D., 2010. Approaching routine 2π/1000 phase resolution for off-axis type holography. Ultramicroscopy 110, 447–459. https://doi.org/10.1016/J.ULTRAMIC.2009.11.017
Yamasaki, Y., Teramoto, Y., Yoshikawa, K., 2001. Disappearance of the Negative Charge in Giant DNA witha Folding Transition. Biophysical Journal 80, 2823–2832. https://doi.org/10.1016/S0006-3495(01)76249-2
Yap, M.L., Rossmann, M.G., 2014. Structure and function of bacteriophage T4. Future Microbiology 9, 1319–1337. https://doi.org/10.2217/fmb.14.91
Yesibolati, M.N., Laganà, S., Sun, H., Beleggia, M., Kathmann, S.M., Kasama, T., Mølhave, K., 2020. Mean Inner Potential of Liquid Water. Phys. Rev. Lett. 124, 065502. https://doi.org/10.1103/PhysRevLett.124.065502
Zivanovic, Y., Confalonieri, F., Ponchon, L., Lurz, R., Chami, M., Flayhan, A., Renouard, M., Huet, A., Decottignies, P., Davidson, A.R., Breyton, C., Boulanger, P., 2014. Insights into Bacteriophage T5 Structure from Analysis of Its Morphogenesis Genes and Protein Components. https://doi.org/10.1128/JVI.02262-13